Materials Science & Engineering A 869 (2023) 144805

Contents lists available at ScienceDirect

Materials Science & Engineering A

journal homepage: www.elsevier.com/locate/msea

In-situ micro-cantilever bending studies of a white etching layer thermally induced on rail wheels

M. Freisinger [a,c,*], L. Zauner [b], R. Hahn [b], H. Riedl [b,c], P.H. Mayrhofer [c]

[a] AC2T Research GmbH, A-2700, Wiener Neustadt, Austria
[b] Christian Doppler Laboratory for Surface Engineering of High-performance Components, TU Wien, Austria
[c] Institute of Materials Science and Technology, TU Wien, Austria

ARTICLE INFO

Keywords:
Rail-wheel contact
White etching layer
Micromechanical properties
J-integral

ABSTRACT

A complex and untraceable mechanical and thermal loading situation in rolling-sliding contacts can lead to the formation of white etching layers (WELs), depicting critical crack initiation sites. For our detailed studies, to obtain a holistic view of the microstructural characteristics and micro-mechanical properties, we prepared a WEL on a decommissioned (after 200,000 km service life) rail wheel by laser surface treatments with a defined energy input. This WEL is predominantly martensitic down to a depth of 30–40 μm, after which a transition to the deformed ferritic-pearlitic microstructure of the hypoeutectoid rail wheel steel is present. The martensitic region is with 6.98 ± 0.68 GPa significantly harder than the transition zone (5.17 ± 0.39 GPa) and the deformed ferritic-pearlitic base material (3.30 ± 0.33 GPa). *In-situ* V-notched micro-cantilever bending experiments of the martensitic (and thus most brittle) region show crack initiation and propagation – mostly along the boundaries of the martensitic grains – besides a plastic behavior. Applying the elastoplastic fracture mechanics allows to derive the local fracture toughness K_{JQ}, which is 16.4 ± 1.2 MPam$^{1/2}$ for this martensitic region of the WEL. The results outpoint the application of micro-cantilever bending tests in addition to hardness testing as a promising tool to discuss the relationship of microstructural characteristics with its micro-mechanical properties.

1. Introduction

As one of the most common structural materials over several decades, understanding the damage patterns and failure of steels in engineering applications is still a significant issue for material science. Contact fatigue failure represents an important economic and safety issue, for instance, in bearings, rails, and wheels [1–4], and is strongly affected by near-surface microstructural changes. Hypoeutectoid steels are prone to form a so-called white etching layer (WEL), a nano-crystalline layer appearing white under light optical microscopy after etching with a nitric acid. The formation process is still in discussion, predominantly described due to severe mechanical and/or thermal loads [5–11]. Especially in rolling-sliding contacts, there are numerous variations of so-called WELs occurring [8,12–15] due to a complex time- and location-dependent loading situation. WEL-like microstructures are prominent crack initiation sites where cracks usually propagate perpendicular to the surface through the WEL or at the interface between the WEL and the underlying material [16–21]. This is associated with the commonly assumed brittle behavior of white etching layers. However, studies on the mechanical properties of WEL-like microstructures going beyond hardness evaluation are scarce due to the non-applicability of conventional testing of such small-scale features. Recent studies from A. Kumar et al. [8] and A.K. Saxena et al. [22] presented the first correlation between microstructural evolution and fracture characteristics of white etching layers formed on pearlitic rail steel during service. Based on spatially resolved sample preparation by focused ion beam (FIB) technology, micro-mechanical testing of distinct microstructural features is an interesting approach to gain a more detailed understanding on elasto-plastic material response [23,24]. *In-situ* micromechanical testing is well established for brittle materials such as single crystals and hard coatings [25–28], where linear elastic fracture mechanics (LEFM) can be applied. For materials exhibiting a significant plastic zone at the crack tip (semi-brittle/ductile materials), the elastoplastic fracture mechanics (EPFM) must be applied, which is less established for micro-scale mechanical testing [29,30].

Damage and failure of rail wheels – typically affected by near-surface microstructural changes and refereed to the formation of WEL domains – demands detailed knowledge about the microstructure's fracture

* Corresponding author. AC2T Research GmbH, A-2700, Wiener Neustadt, Austria.
E-mail address: matthias.freisinger@ac2t.at (M. Freisinger).

https://doi.org/10.1016/j.msea.2023.144805
Received 13 January 2023; Received in revised form 14 February 2023; Accepted 15 February 2023
Available online 16 February 2023

behavior and toughness [2,31–35]. To improve the understanding on WEL-affected failure mechanisms, qualitative and quantitative analysis of their fracture behavior is essential. Detailed data sets are also of utmost importance for modelling approaches. Currently, no data on fracture behavior and local fracture toughness of WEL on rail wheels are available.

This study applies a holistic approach to characterize the microstructure of a WEL thermally induced by laser surface treatment with defined and reproducible energy input of a decommissioned hypoeutectoid rail wheel steel as well as their mechanical properties, particularly hardness and fracture toughness. The latter is also quantitatively evaluated with *in-situ* micro-mechanical bending experiments and applying EPFM.

2. Materials and methods

2.1. Materials

The hypoeutectoid steel chosen within this work is the rail wheel steel grade ER7 (Table 1). To picture the degree of deformation of a near-surface microstructure in service, the Austrian Federal Railways provides an ex-service rail wheel with a mileage of ~200,000 km. The wheel (diameter of 0.95 m) is cut by a conventional band saw. The preparation of the wheel tread surface includes the removal of rust by gentle hand-grinding with a SiC #1000 paper (18 μm grain size) and additionally a careful Fe(III)Cl etching to identify possible WEL induced during service. A laser surface treatment is conducted on regions obtaining no WEL from service to thermally induce a WEL with a distinct thermal loading on the deformed microstructure. A Direct Diode Laser System (HighLight 8000D, Coherent, U.S.) with a rectangular laser spot (3 × 24 mm) is used at a constant travel speed of 12 mm/s. To induce a WEL with a thickness of ~30 μm, the laser parameters used within this work are based on a previous work [36]. The average energy density is 3.74 J/mm^2 with a pre-set surface temperature of 640 °C, measured by an externally mounted pyrometer (LPC03, Mergenthaler, Germany). Out of this laser-treated region, samples in size of ~5 × 5x5 mm^3 are cut out using a laboratory cutting device (Struers Secotom-50; Struers ApS, Denmark) and subsequently mechanically polished.

2.2. Microstructural characterization

Characterization of the microstructure is executed by light optical microscopy (LOM) (Axio Imager M2m, Carl Zeiss AG, Germany) as well as by scanning electron microscopy (SEM) (Jeol JIB 4700F, Jeol Ltd., Japan). The latter is equipped with a Schottky field emission gun, secondary and backscattered electron detectors, and an electron backscatter diffraction (EBSD) detector (Bruker e-Flash HR, USA). The corresponding samples are prepared by embedding small pieces in conductive compounds. After the metallographic sample preparation to a mirror-polished surface quality (1 μm diamond fine polishing), the cross-sectional cuts are etched with diluted nitric acid (3% HNO_3, 97% ethanol). SEM investigations are performed at 15 kV acceleration voltage and 10 pA probe current. For the EBSD measurements, the samples are embedded in an advanced embedding compound [39], and the surface quality was further improved by additional finish polishing (colloidal Silica <0.25 μm). The parameters used for the EBSD investigations are 15 kV acceleration voltage, 3.6 nA probe current, 16 mm working distance, and 18 mm detector distance. The Kikuchi patterns, acquired at 240 × 160 px with an exposure time of 40 ms, are analyzed with the Bruker Esprit 2.2 software package using the AMCSD database for phase identification.

2.3. Micro-mechanical investigations

Vickers hardness depth profiles are executed with a load of 0.05 kp (0.49 N), indenting the cross-sections at increasing distances from the surface with a Future-Tech FM-700 hardness tester. The diagonals of the indents are measured with a LOM. Further, nanoindentation measurements are performed with a Bruker Hysitron Triboindenter TI980 – Performech II (equipped with a Berkovich diamond tip) to address hardness and Young's modulus, an array of 5 × 5 indents was performed for each zone. The load-displacement curves (with a peak load of 5 mN) were evaluated, and hardness was deduced via the load/area ratio, whereby the reduced Young's modulus was evaluated via the Oliver and Pharr method [40].

To evaluate fracture toughness, *in-situ* micro-cantilever bending experiments are carried out using the geometrical relations depicted in Fig. 1. Cantilevers are milled by a focused ion beam (FIB) on the edge of the ~5 × 5x5 mm^3 samples. A scanning electron microscopy (SEM) equipped with FIB (Jeol JIB 4700F Multi Beam System, Jeol Ltd., Japan) is used with 30 keV Ga^+ ions to create eight cantilevers on the sample. FIB milling starts with coarse milling at 10 nA and a dose of 100 nC/μm^2, followed by fine milling at 1 nA||8 nC/μm^2. Straight through-thickness notches with a final notch depth of ~1.2 μm are made at 10 nA||8 nC/μm^2. The last cantilever preparation step is polishing the side surfaces at 300 pA||5 nC/μm^2 to avoid side-notch effects. The cantilevers have a rectangular cross-section with lengths of ~25 μm, whereby the ratio of cantilever length (L'):height (w):breadth (b) is about 5:1:1 [41].

The micromechanical experiments are performed using a Femto-Tools FT-NMT04 *in-situ* nanoindentation system built in a Zeiss Sigma 500 VP SEM. A detailed depiction of the intender tip above the laser-treated steel surface is depicted in Fig. 2a. The nanoindenter is

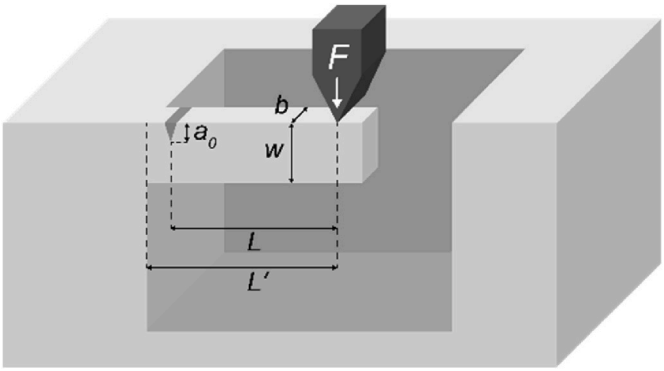

Fig. 1. Schematic overview of the micro-cantilever prepared by FIB milling with the diamond wedge applying the load at a distance L from the notch.

Table 1
Material properties of the steel grade ER7 according to the standard EN13262 [37].

C	Si	Mn	P	S	Cr	Cu	Mo	Ni	V	Cr + Mo + Ni
[wt%]										
0.52	0.40	0.80	0.020	0.015	0.30	0.30	0.08	0.30	0.06	0.50

R_{eH}	R_m	A_5	Minimum Hardness	K_Q (CT specimens [38])
[N/mm^2]	[N/mm^2]	[%]	[HV10]	[MPa m$^{1/2}$]
≥520	820–940	≥14	260	40–80

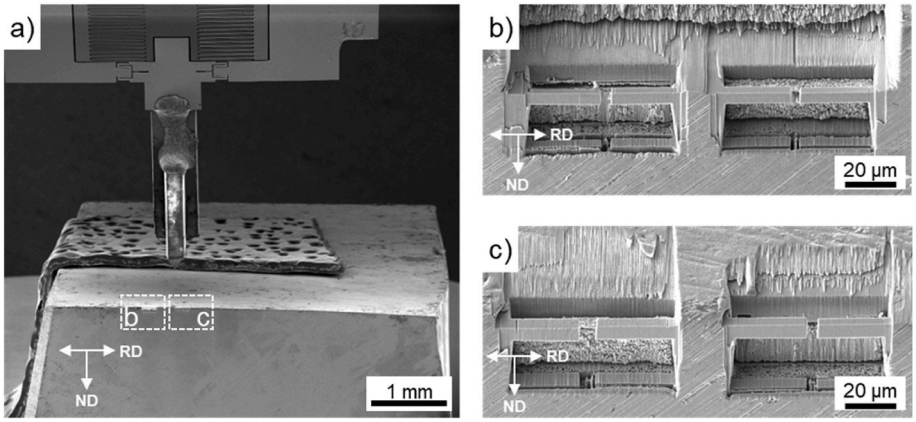

Fig. 2. (a) Cube cut-out of the laser-treated steel surface as placed inside the SEM chamber, with the diamond wedge of the nanoindentation system approaching from the top. Details of the FIB milled cantilevers – marked in (a) with rectangles – are shown in (b) and (c) before testing.

equipped with a diamond wedge (tip length ~10 µm), and after careful alignment of the samples, they are loaded in a displacement-controlled mode at a speed of 20 nm s^{-1} and a distance L from the notch (Fig. 1). The intended crack plane is normal to the rolling direction (ND) of the wheel (Fig. 2b and c). A sinusoidal signal is superimposed (at an amplitude of 5 nm and a frequency of 200 Hz, continuous stiffness measurement CSM) to record the force F, displacement u, and stiffness k of the cantilever during the measurement.

Since the materials experienced extensive plastic deformation during the bending tests, the evaluation was performed according to the elastic-plastic fracture behavior in the context of the J-integral. A detailed explanation of the conducted analytical procedure and an alternative data evaluation can be found in works by Alfreider et al. [42–45].

The J-integral as proposed by Rice was used for our analysis [46]:

$$J_n = \frac{2A_{tot,n}}{b(w-a_n)} \tag{1}$$

where J_n is the J-integral corresponding to data point n, $A_{tot,n}$ is the area under the force-displacement curve (F-u) up to point n, a_n denotes the crack length at point n, and b as well as w are geometric parameters as described above. $A_{tot,n}$ is calculated after:

$$A_{tot,n} = \int_0^{u_n} F\, du \tag{2}$$

The calculation of the current crack length is conducted using the recorded cantilever stiffness k following:

$$\int_0^{a_n} \frac{a}{w} Y\left(\frac{a}{w}\right)^2 da = \frac{\left(\frac{k_o}{k_n}-1\right)L^3}{18\pi(1-\nu^2)L'^2} \tag{3}$$

where $Y\left(\frac{a}{w}\right)$ is a dimensionless shape factor proposed by Riedl et al. [47], ν denotes Poisson's ratio (chosen as 0.3 for all calculations), k_o is the stiffness of the unnotched cantilever, whereas k is the stiffness of the notched cantilever at point n. Furthermore, k_o can be calculated from the steady state stiffness value $k(a_0)$ where proper contact between cantilever and indenter tip is established, yet without any crack propagation:

$$k_0 = k(a_0)\left(1 + \frac{18\pi(1-\nu^2)L'^2}{L^3}\int_0^{a_0} \frac{a}{w} Y\left(\frac{a}{w}\right)^2 da\right) \tag{4}$$

By plotting the J-integral vs. the crack propagation Δa (crack resistance curve) the J_Q can be obtained by the criteria of Wurster et al. [48]. This approach states that the blunting of the artificial FIB milled notch starts to initiate a natural crack with stable crack growth at a crack propagation Δa of 0.5 µm. Finally, the fracture toughness K_{IQ} can be calculated:

$$K_{IQ} = \sqrt{J_Q \frac{E}{(1-\nu^2)}} \tag{5}$$

All calculations were conducted using a self-written MATLAB script (The MathWorks Inc., version R2019b, Natick, Massachusetts).

3. Results

Due to the laser surface treatment, the surface is blue-greyish with darker regions marking the border of the laser track (Fig. 3a). Cross-sectional cuts in transversal direction (CS-TD) and rolling direction (CS-RD) are given in Fig. 3b and c, respectively. At the very top of the laser track, a thin oxide layer is present, which is responsible for the colored surface. A WEL formed down to a depth of 30–40 µm from the surface, which already in these lower magnification SEM images looks martensitic-based. Further more, detailed cross-sectional SEM investigations in transversal direction (Fig. 4a, b, c, d, e) and rolling direction (Fig. 4f, g, h, i, j) confirm the martensitic structure at the top region, followed by a gradual transition towards the base material with increasing distance from the surface. The martensitic-based top region of the WEL is fine-grained and randomly orientated (with acicular-like martensite gains) both in the transversal as well as in the rolling direction, Fig. 4b and c, respectively. Further down from the surface (30–40 µm) also randomly distributed ferrite grains are present. After this, at a distance of 40–50 µm from the surface, the microstructure contains a mixture of martensite, deformed ferrite, and pearlite grains, again very similar for the transversal as well as rolling direction, Fig. 4c and h, respectively. Underneath this gradual transition zone, the microstructure is deformed ferritic-pearlitic with slightly more alignment in transversal direction (Fig. 4d) than in rolling direction (Fig. 4i). The almost undeformed virgin ferritic-pearlitic microstructure in both directions is given in Fig. 4e and j. These cross-sections taken at a distance of ~1 cm from the surface exhibit a globular ferritic-pearlitic microstructure without deformation signs and without a specific alignment.

Inverse pole figure (IPF) maps of the EBSD analysis from the cross-section in transversal direction highlight the massive grains-size difference between the outer-most martensitic structure of the WEL, the transition zone, and the deformed ferritic-pearlitic microstructure underneath, see Fig. 5a. The individual misorientations of the grains is evaluated by applying a 3 × 3 kernel (Fig. 4b), resulting in an average kernel average misorientation (KAM) angle of 1–2° for the ferritic-pearlitic microstructure. The KAM angle within the WEL seems to be larger. However, no quantitative analysis was possible due to small grain size within this region.

Representative low-load Vickers hardness measurements for these

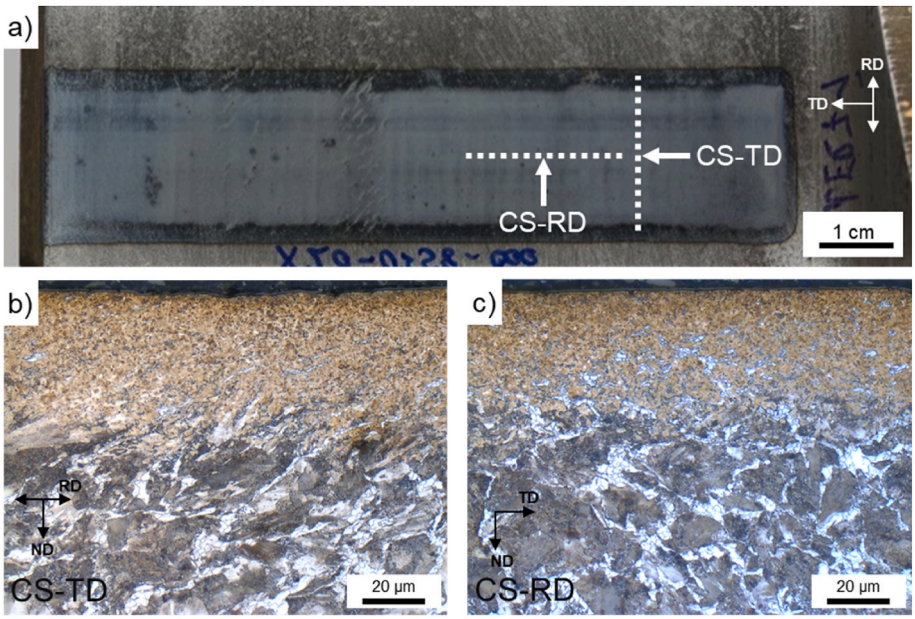

Fig. 3. (a) Top-view of the rail wheel tread surface with the track of the laser surface treatment. LOM images of the cross-sectional cut in transversal direction (CS-TD, (b)) and in rolling direction (CS-RD, (c)) picture the martensitic WEL, the transition zone, and the ferritic-pearlitic underlying microstructure. CS-TD shows a weak alignment of the deformed microstructure.

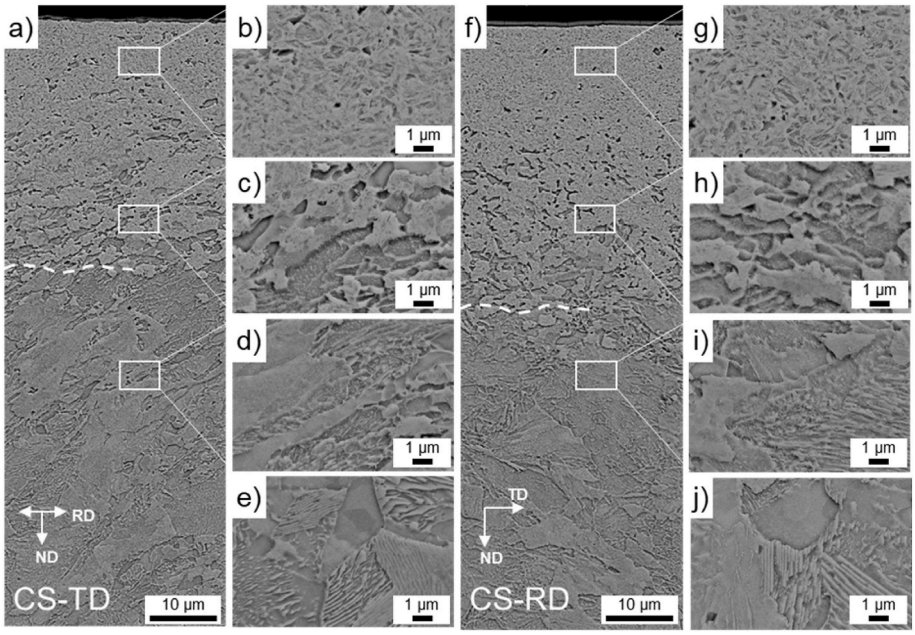

Fig. 4. Electron backscattered images representing the cross-sectional cut in transversal direction (CS-TD, (a)) and rolling direction (CS-RD, (f)). Insets with higher magnification images show the WEL (b, g), the transition zone (c, h), the underlying deformed microstructure (d, i), and the undeformed bulk microstructure (e, j).

regions yield 739 ± 34 HV0.05 within the martensitic dominated topmost region and 516 ± 11 HV0.05 for the transition zone of the WEL, while the deformed ferritic-pearlitic microstructure underneath exhibits 308 ± 16 HV0.05. Nanoindentations from these zones yield 6.98 ± 0.68 and 5.17 ± 0.39 GPa for the martensitic dominated and the transition zone of the WEL, respectively, whereas the deformed ferritic-pearlitic microstructure yields 3.30 ± 0.33 GPa. Thus, confirming the observed trend of the low-load Vickers hardness measurements. Fig. 5c shows the areas within these regions where these measurements were conducted, in addition to the obtained hardness values.

In-situ bending experiments of V-notched micro-cantilevers taken out from the martensitic-dominated top region of the WEL are conducted to evaluate its fracture behavior qualitatively and to determine its fracture toughness value. Out of eight cantilevers tested, six (C-2, -3, -4, -6, -7, -8) provided valid fracture experiments. Their stress-displacement curves calculated from the recorded force-displacement signals are given in Fig. 6a. These clearly show, after an initial linear behavior, a plastic behavior, followed by a region with features characteristic for crack initiation and propagation. Although the maximum stress scatters between ~70 and 100 mN/mm^2, which could also originate from errors of the cross-section measurements, their fracture behavior shows nearly no differences during the *in-situ* studies, which are exemplarily shown in Fig. 6b, c, and d for the cantilevers C-2, C-4, and C-8, respectively.

Crack initiation and propagation lead to a decrease in stiffness of the

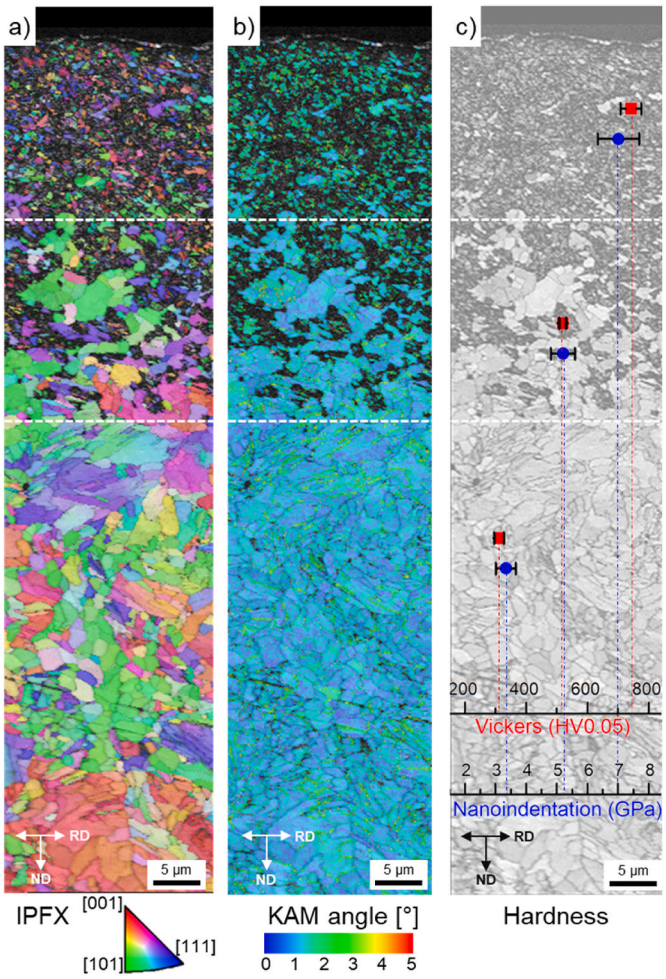

Fig. 5. The EBSD measurements are performed on the cross-sectional cut in transversal direction (CS-TD) and include the WEL with low pattern quality and a high fraction of zero-solutions, the transition zone, and the underlying deformed hypoeutectoid steel. The inverse pole figure (IPFX) map (a) and the Kernel average misorientation (KAM) angle map (b) is shown. In (c), the hardness values within the three zones evaluated by the low-load Vickers technique and nanoindentation are presented.

cantilever (Fig. 7a) from which the crack propagation can be calculated (Fig. 7b) using a constant elastic modulus. This is used to obtain the evolution of the J-integral during the crack propagation (Fig. 7c), which shows similar curves for the individual cantilevers. Their evaluation yields fracture toughness values K_{IQ} of 16.4 ± 1.2 MPam$^{1/2}$.

Exemplarily, Fig. 8 shows detailed SEM studies of the two cantilevers C-2 (Fig. 8a, b and c) and C-6 (Fig. 8d, e and f) after the bending experiment. These clearly show the propagating crack from the FIB milled pre-notch of the sample. Because at the sidewalls of the cantilevers only a plain-stress situation is active (contraction is allowed), the plastic deformation zone at these surfaces is typically 9-times (when using a Poisson's ratio of 1/3) of that within the center of the sample where essentially a plain-strain situation is active (contraction is hindered). The contraction of the side walls of the cantilevers can nicely be seen in the SEM images for the samples C-2 (Fig. 8a) and C-6 (Fig. 8d). FIB milling the cantilever at the region of the crack propagation down to its center allows to observe the area of a plain-strain situation. For this, the opened crack was filled with tungsten to protect the surface during FIB milling, Fig. 8b shows the sample C-2 and Fig. 8e sample C-6. Especially the latter shows a clear crack deflection, which can be related to the microstructural features of this sample, which are better seen during ion channeling contrast imaging Fig. 8f. These investigations suggest that the crack is deflected at the individual grain and phase boundaries of the acicular martensite. In this region, at the crack tip, the sample C-2 shows fewer zig-zag arrangements of martensite grains (Fig. 8c), thus the crack propagation is little deflected. These differences in crack propagation can account for the higher (even highest) J values of sample C-6, see Fig. 7c.

4. Discussion

Laser surface treatments are commonly used to create WELs to improve wear resistance of steel surfaces or to imitate the near-surface microstructures present due to rail-wheel contacts [12–16]. Such WELs are often termed "thermal WELs" to indicate their origin, since under certain parameters WEL-like microstructures can also be formed mechanically [49]. In both cases, the WEL is frequently the origin of many crack initiations, and its brittle nature only provides a limited resistance against crack growth. Recently we showed that the microstructural characteristics of laser-induced thermal WELs on deformed wheel steel surfaces are comparable to WELs formed on a rail wheel tread surfaces during railway operation [36]. Essential is, that a deformed wheel steel is used, as the same laser treatment of an undeformed wheel steel base material leads to a "thermal WEL" with significantly different microstructural features as compared to the "field WEL" [36]. This motivated us to prepare "thermal WELs" with significant thickness and areal expansion on a deformed decommissioned rail wheel, to allow for detailed microstructural characterizations and FIB machining of eight microcantilevers used for *in-situ* micromechanical investigations. In contrast to investigations on WELs from field with estimated loading history, the artificial formation by laser surface treatments serves as a defined and reproducible approach to imitate WELs in terms of their energy and temperature input, respectively. These allowed for a holistic view of the microstructural characteristics and the mechanical properties (here especially strength and fracture toughness) of the WEL, which is needed to understand the fracture behavior of this most sensitive region.

The thermal WEL, which is induced on a deformed rail wheel by laser surface treatments, is characterized by a 30–40 µm thick outer-most martensitic-based region and a 20–30 µm wide transition zone to the deformed ferritic-pearlitic microstructure of the hypoeutectic steel. The 739 ± 34 HV0.05 respectively 6.98 ± 0.68 GPa hardness of the martensitic region of the WEL compares well to those of WELs on rails, with hardness values of ~700–800 HV0.05 respectively ~7 GPa [15, 50–52]. When it comes to fracture toughness – which strongly depends on microstructural characteristics and often shows an inverse correlation with hardness [53] – in-depth studies are quite rare [22,54–56]. Often, only semi-empirical descriptors are used to estimate the fracture toughness based on hardness values. But besides uncertain estimations, which make such fracture toughness evaluations demanding [24], toughness and hardness often go separate ways, as mentioned above. Thus, qualitative and quantitative evaluations of the fracture behavior of such WELs are needed. Kumar et al. [56] pioneered the experimental study, by *in-situ* micromechanical investigations, of the fracture toughness of a WEL formed during service on a R350HT rail steel (Fe-0.72C-1.1Mn-0.56Si-0.11Cr (wt.%)). They report about fracture toughness values of 21.5 ± 3.0 to 25.4 ± 2.3 MPam$^{1/2}$ and a hardness of 1000–700 HV0.025. While the hardness values are comparable, the fracture toughness values are much higher than the 16.4 ± 1.2 MPam$^{1/2}$ obtained in this work. This might originate from the different chemical composition of the steel grade and the deformation state, but also the different approach for evaluating the stiffness and J-integral. Kumar et al. used unloading cycles to evaluate the stiffness change and estimated the J-integral by intersection of the blunting line and the stable crack growth, whereas we used a superimposed sinusoidal signal with an amplitude of 5 nm and a frequency of 200 Hz and obtained the J-integral at a crack propagation Δa of 0.5 µm according to Wurster et al. [48]. Our results are in good agreement with the results of Saxena et al. [22],

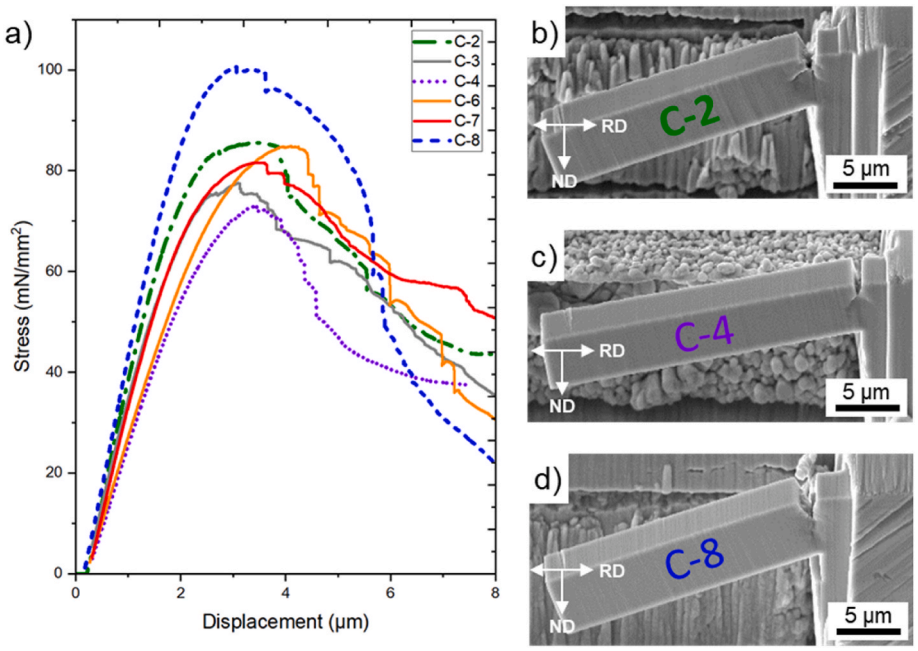

Fig. 6. (a) Stress-displacement curves for all seven valid tested micro-cantilevers show elastic deformation at the beginning, followed by plastic deformation, crack initiation, and propagation. SEM images of representative cantilevers prove this after testing, where cantilever C-2 (b) shows maximum stress of ~85 N/mm^2, cantilever C-4 (c) with the lowest (~72 N/mm^2), and cantilever C-8 (d) reveals the highest maximum stress of ~100 N/mm^2.

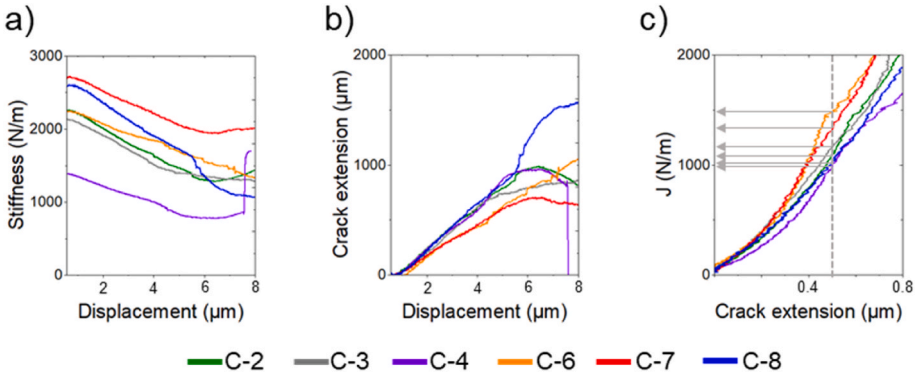

Fig. 7. Based on each cantilever's stiffness change (a), the crack extension is calculated (b). To determine the *J*-integral, the crack resistance curve (c) is plotted where J_Q is determined at a crack extension of 0.5 µm.

where a WEL from a R350HT rail and a lab-simulated martensite reveal 14.4 ± 1.1 MPam$^{1/2}$ and 16.9 ± 1.2 MPam$^{1/2}$ by using the same toughness criteria to estimate the J-integral.

Detailed microstructural investigations – especially after the fracture experiments, Fig. 8 – allowed to explain the deviating J-integral values using the samples C-2 and C-6 (Fig. 7). Thereby, the rather high J-integral values of C-6 could be related to the more pronounced crack deflection at the boundaries of the more acicular-like martensite grains, resulting in calculated fracture toughness values of ~18 MPam$^{1/2}$. In contrast, the fracture toughness calculated for C-2 is ~16 MPam$^{1/2}$. As these results suggest, comparing localized micro-mechanical testing needs to be done with caution, as differences in local morphology and stress state easily influence the results, especially if the grain size of certain structures is in the range of the specimen geometry. Despite the experimental challenges [24], the quantitative as well as qualitative results from the micro-mechanical testing of the martensitic-based region of the WEL thermally induced by surface laser treatment of a hypoeutectoid steel are in good agreement with the rare literature about micro-mechanical testing of WELs on rail steels from the field [22,56]. Besides well-established microstructural characterization methods and micro-hardness testing methods, this work underlines the need for micro-cantilever bending experiments to characterize the fracture behavior and evaluate the fracture toughness. A holistic view of the various mechanical properties is required, since toughness cannot be estimated without error from hardness and microstructure, but is essential to understand small-scale microstructural phenomena prone to crack initiation, growth, and failure [57–59].

5. Conclusions

Within this work, the microstructure of a thermal WEL induced by laser surface treatment with defined thermal loading parameters and a pre-deformation state from the rail-wheel contact is investigated in terms of microstructural and micro-mechanical characteristics.

This thermal WEL contains a fine-grained, randomly orientated acicular martensitic microstructure with an increasing fraction of ferrite islands from the surface towards the transition to the underlying deformed ferritic-pearlitic microstructure. The 30–40 µm thick outermost martensitic-based region exhibits a hardness of 739 ± 34 HV0.05 respectively 6.98 ± 0.68 GPa while the 20–30 µm wide transition zone

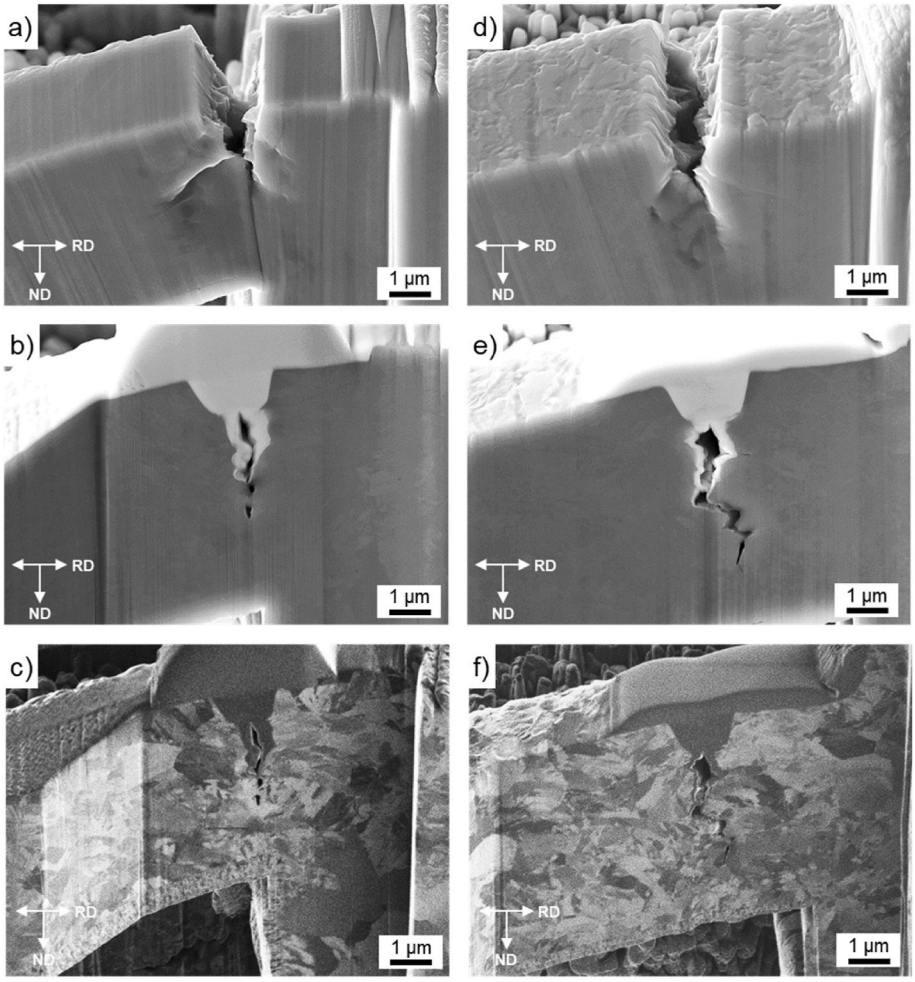

Fig. 8. In the first row, secondary electron (SE) images of the fractured cantilever C-2 (a) and C-6 (d) are presented. The cantilevers reveal the same stress level during bending but different J_Q values. After depositing tungsten onto the notch region to protect the cantilever, FIB milling is done to prepare a cross-section in the middle of the cantilever, displayed in the second row (b, e). Ion channeling contrast images are shown additionally (c, f) to highlight the crack evolution within the microstructure.

shows 516 ± 11 HV0.05 respectively 5.17 ± 0.39 GPa, and the deformed ferritic-pearlitic microstructure yields 308 ± 16 HV0.05 respectively 3.30 ± 0.33 GPa. Detailed microstructural investigations in combination with *in-situ* V-notched micro-cantilever bending experiments show that crack propagation is preferred at the boundaries of the acicular martensite grains. The generally elastic-plastic fracture behavior required the evaluation with the *J*-integral, obtained by continuous stiffness measurement, yielding K_{IQ} of 16.4 ± 1.2 MPam$^{1/2}$. It is shown that the application of micro-cantilever bending tests is a promising tool to describe the micro-mechanical properties in addition to common nanoindentation, instead of unprecise estimations of the fracture toughness based on obtained hardness values. The improvements in the field of micro-testing enables a holistic view of micro-mechanical properties, especially hardness and toughness, in relation to its microstructural characteristics.

CRediT authorship contribution statement

M. Freisinger: Conceptualization, Methodology, Validation, Writing – original draft. **L. Zauner:** Software, Data curation, Writing – review & editing. **R. Hahn:** Methodology, Data curation, Writing – review & editing. **H. Riedl:** Supervision, Writing – review & editing. **P.H. Mayrhofer:** Supervision, Writing – review & editing.

Declaration of competing interest

The authors declare that they have no known competing financial interests or personal relationships that could have appeared to influence the work reported in this paper.

Data availability

Data will be made available on request.

Acknowledgments

This project has received funding from the Shift2Rail Joint Undertaking (JU) under grant agreement No 826255 and No 101012456. The JU receives support from the European Union's Horizon 2020 research and innovation program and the Shift2Rail JU members other than the Union. In addition, this work was funded by the "Austrian COMET-Program" (project InTribology1, no. 872176) via the Austrian Research Promotion Agency (FFG) and the federal states of Niederösterreich and Vorarlberg and was carried out within the "Excellence Center of Tribology" (AC2T research GmbH). The financial support by the Austrian Federal Ministry for Digital and Economic Affairs, the National Foundation for Research, Technology and Development, and the Christian Doppler Research Association is gratefully acknowledged (Christian Doppler Laboratory "Surface Engineering of high-performance Components").

References

[1] X. Jin, Y. Chen, L. Wang, H. Han, P. Chen, Failure prediction, monitoring and diagnosis methods for slewing bearings of large-scale wind turbine: a review, Measurement 172 (Feb. 2021), 108855, https://doi.org/10.1016/j.measurement.2020.108855.

[2] C. Suetrong, Investigations of fatigue crack propagation in ER8 railway wheel steel with varying microstructures, Mater. Sci. 17 (2022).
[3] Y. Liu, B. Stratman, S. Mahadevan, Fatigue crack initiation life prediction of railroad wheels, Int. J. Fatig. 28 (7) (Jul. 2006) 747–756, https://doi.org/10.1016/j.ijfatigue.2005.09.007.
[4] H.C. Eden, J.E. Garnham, C.L. Davis, Influential microstructural changes on rolling contact fatigue crack initiation in pearlitic rail steels, Mater. Sci. Technol. 21 (6) (Jun. 2005) 623–629, https://doi.org/10.1179/174328405X43207.
[5] C. Liu, et al., Formation mechanism for the white etching microstructure in the subsurface of the failure pearlite wheel steel, Wear 494 (495) (Apr. 2022), 204243, https://doi.org/10.1016/j.wear.2022.204243.
[6] C. Bernsteiner, et al., Simulation and experiment based investigations of squat formation mechanisms, Wear 440–441 (2019), 203093, https://doi.org/10.1016/j.wear.2019.203093.
[7] A. Al-Juboori, et al., Characterisation of White Etching Layers formed on rails subjected to different traffic conditions, Wear 436 (437) (Oct. 2019), 202998, https://doi.org/10.1016/j.wear.2019.202998.
[8] A. Kumar, G. Agarwal, R. Petrov, S. Goto, J. Sietsma, M. Herbig, Microstructural evolution of white and brown etching layers in pearlitic rail steels, Acta Mater. 171 (Jun. 2019) 48–64, https://doi.org/10.1016/j.actamat.2019.04.012.
[9] M. Shamsujjoha, Evolution of microstructures, dislocation density and arrangement during deformation of low carbon lath martensitic steels, Mater. Sci. Eng., A 776 (Mar. 2020), 139039, https://doi.org/10.1016/j.msea.2020.139039.
[10] J.I. Pereira, G. Tressia, E.J. Kina, A. Sinatora, R.M. Souza, Analysis of subsurface layer formation on a pearlitic rail under heavy haul conditions: spalling characterization, Eng. Fail. Anal. 130 (Dec. 2021), 105549, https://doi.org/10.1016/j.engfailanal.2021.105549.
[11] G. Baumann, H.J. Fecht, S. Liebelt, Formation of white-etching layers on rail treads, Wear 191 (1–2) (Jan. 1996) 133–140, https://doi.org/10.1016/0043-1648(95)06733-7.
[12] S. Li, J. Wu, R.H. Petrov, Z. Li, R. Dollevoet, J. Sietsma, Brown etching layer": a possible new insight into the crack initiation of rolling contact fatigue in rail steels? Eng. Fail. Anal. 66 (Aug. 2016) 8–18, https://doi.org/10.1016/j.engfailanal.2016.03.019.
[13] M. Messaadi, M. Steenbergen, Stratified surface layers on rails, Wear 414–415 (Nov. 2018) 151–162, https://doi.org/10.1016/j.wear.2018.07.019.
[14] Q. Lian, et al., Evolution of thermally induced white etching layer at rail surface during multiple wheel/train passages, Int. J. Fatig. 159 (Jun. 2022), 106799, https://doi.org/10.1016/j.ijfatigue.2022.106799.
[15] Y.Z. Chen, C.G. He, X.J. Zhao, L.B. Shi, Q.Y. Liu, W.J. Wang, The influence of wheel flats formed from different braking conditions on rolling contact fatigue of railway wheel, Eng. Fail. Anal. 93 (Nov. 2018) 183–199, https://doi.org/10.1016/j.engfailanal.2018.07.006.
[16] B. Hieu Nguyen, A. Al-Juboori, H. Zhu, A.A. Gazder, H. Li, K. Tieu, Fracture mechanisms in rails with mechanically and thermomechanically-induced white etching layers under three-point bending, Eng. Fail. Anal. 131 (Jan. 2022), 105813, https://doi.org/10.1016/j.engfailanal.2021.105813.
[17] Q. Lian, et al., Crack propagation behavior in white etching layer on rail steel surface, Eng. Fail. Anal. 104 (Oct. 2019) 816–829, https://doi.org/10.1016/j.engfailanal.2019.06.067.
[18] A. Al-Juboori, et al., Squat formation and the occurrence of two distinct classes of white etching layer on the surface of rail steel, Int. J. Fatig. 104 (Nov. 2017) 52–60, https://doi.org/10.1016/j.ijfatigue.2017.07.005.
[19] S. Pal, W.J.T. Daniel, M. Farjoo, Early stages of rail squat formation and the role of a white etching layer, Int. J. Fatig. 52 (Jul. 2013) 144–156, https://doi.org/10.1016/j.ijfatigue.2013.02.016.
[20] R.I. Carroll, J.H. Beynon, Rolling contact fatigue of white etching layer: Part 1 Crack morphology, Wear 262 (2007) 1253–1266, https://doi.org/10.1016/j.wear.2007.01.003.
[21] C.J. Rasmussen, S. Fæster, S. Dhar, J.V. Quaade, M. Bini, H.K. Danielsen, Surface crack formation on rails at grinding induced martensite white etching layers, Wear 384–385 (Aug. 2017) 8–14, https://doi.org/10.1016/j.wear.2017.04.014.
[22] A.K. Saxena, A. Kumar, M. Herbig, S. Brinckmann, G. Dehm, C. Kirchlechner, Micro fracture investigations of white etching layers, Mater. Des. 180 (Oct. 2019), 107892, https://doi.org/10.1016/j.matdes.2019.107892.
[23] G. Dehm, B.N. Jaya, R. Raghavan, C. Kirchlechner, Overview on micro- and nanomechanical testing: new insights in interface plasticity and fracture at small length scales, Acta Mater. 142 (Jan. 2018) 248–282, https://doi.org/10.1016/j.actamat.2017.06.019.
[24] R. Pippan, S. Wurster, D. Kiener, Fracture mechanics of micro samples: fundamental considerations, Mater. Des. 159 (Dec. 2018) 252–267, https://doi.org/10.1016/j.matdes.2018.09.004.
[25] B.N. Jaya, C. Kirchlechner, G. Dehm, Can microscale fracture tests provide reliable fracture toughness values? A case study in silicon, J. Mater. Res. 30 (5) (Mar. 2015) 686–698, https://doi.org/10.1557/jmr.2015.2.
[26] J.P. Best, et al., A comparison of three different notching ions for small-scale fracture toughness measurement, Scripta Mater. 112 (Feb. 2016) 71–74, https://doi.org/10.1016/j.scriptamat.2015.09.014.
[27] R. Hahn, M. Bartosik, R. Soler, C. Kirchlechner, G. Dehm, P.H. Mayrhofer, Superlattice effect for enhanced fracture toughness of hard coatings, Scripta Mater. 124 (Nov. 2016) 67–70, https://doi.org/10.1016/j.scriptamat.2016.06.030.
[28] R. Daniel, et al., Grain boundary design of thin films: using tilted brittle interfaces for multiple crack deflection toughening, Acta Mater. 122 (Jan. 2017) 130–137, https://doi.org/10.1016/j.actamat.2016.09.027.
[29] M. Alfreider, D. Kozic, O. Kolednik, D. Kiener, In-situ elastic-plastic fracture mechanics on the microscale by means of continuous dynamical testing, Mater. Des. 148 (Jun. 2018) 177–187, https://doi.org/10.1016/j.matdes.2018.03.051.
[30] B.N. Jaya, V. Jayaram, Fracture testing at small-length scales: from plasticity in Si to brittleness in Pt, J. Occup. Med. 68 (1) (Jan. 2016) 94–108, https://doi.org/10.1007/s11837-015-1489-2.
[31] O.P. Ostash, V.V. Kulyk, T.M. Lenkovskiy, Z.A. Duriagina, V.V. Vira, T.L. Tepla, Relationships between the fatiguecrack growth resistance characteristicsof a steel and the tread surface damageof railway wheel, Archives of Materials Science and Engineering 2 (90) (Apr. 2018) 49–55, https://doi.org/10.5604/01.3001.0012.0662.
[32] T. Kato, Y. Yamamoto, H. Kato, S. Dedmon, J. Pilch, Effect of fracture toughness on vertical split rim failure in railway wheels, Eng. Fract. Mech. 186 (Dec. 2017) 255–267, https://doi.org/10.1016/j.engfracmech.2017.09.025.
[33] H.P. Rossmanith, F. Loibnegger, R. Huber, Thermomechanical fatigue fracture due to repeated braking of railway wheels, Mater. Sci. 42 (4) (Jul. 2006) 466–475, https://doi.org/10.1007/s11003-006-0102-9.
[34] D. Peng, R. Jones, T. Constable, A study into crack growth in a railway wheel under thermal stop brake loading spectrum, Eng. Fail. Anal. 25 (Oct. 2012) 280–290, https://doi.org/10.1016/j.engfailanal.2012.05.018.
[35] A. Ekberg, E. Kabo, Fatigue of railway wheels and rails under rolling contact and thermal loading—an overview, Wear 258 (7–8) (2005) 1288–1300, Mar, https://doi.org/10.1016/j.wear.2004.03.039.
[36] M. Freisinger, et al., Comparative study on the influence of initial deformation and temperature of thermally induced white etching layers on rail wheels, Tribol. Int. 177 (Jan. 2023), 107990, https://doi.org/10.1016/j.triboint.2022.107990.
[37] EN 13262:2004+A2:2011: Railway Applications - Wheelsets and Bogies - Wheels - Product Requirements'.
[38] M. Diener, A. Ghidini, Fracture toughness: a quality index for railway solid wheels, Matls. Perf. Charact. 3 (3) (Jun. 2014), 20130047, https://doi.org/10.1520/MPC20130047.
[39] H. Rojacz, M. Premauer, A. Nevosad, Conductive and edge retaining embedding compounds: influence of graphite content in compounds on specimen's SEM and EBSD performance, Pract. Metallogr. 58 (5) (May 2021) 236–263, https://doi.org/10.1515/pm-2021-0018.
[40] W.C. Oliver, G.M. Pharr, An improved technique for determining hardness and elastic modulus using load and displacement sensing indentation experiments, J. Mater. Res. 7 (6) (Jun. 1992) 1564–1583, https://doi.org/10.1557/JMR.1992.1564.
[41] K. Matoy, et al., A comparative micro-cantilever study of the mechanical behavior of silicon based passivation films, Thin Solid Films 518 (1) (Nov. 2009) 247–256, https://doi.org/10.1016/j.tsf.2009.07.143.
[42] M. Alfreider, S. Kolitsch, S. Wurster, D. Kiener, An analytical solution for the correct determination of crack lengths via cantilever stiffness - SUPP, Mater. Des. 194 (Sep. 2020), 108914, https://doi.org/10.1016/j.matdes.2020.108914.
[43] M. Alfreider, R. Bodlos, L. Romaner, D. Kiener, The influence of chemistry on the interface toughness in a WTi-Cu system, Acta Mater. 230 (May 2022), 117813, https://doi.org/10.1016/j.actamat.2022.117813.
[44] M. Alfreider, J. Zechner, D. Kiener, Addressing fracture properties of individual constituents within a Cu-WTi-SiOx-Si multilayer, J. Occup. Med. 72 (12) (Dec. 2020) 4551–4558, https://doi.org/10.1007/s11837-020-04444-6.
[45] M. Alfreider, D. Kozic, O. Kolednik, D. Kiener, In-situ elastic-plastic fracture mechanics on the microscale by means of continuous dynamical testing, Mater. Des. 148 (Jun. 2018) 177–187, https://doi.org/10.1016/j.matdes.2018.03.051.
[46] X.-K. Zhu, J.A. Joyce, Review of fracture toughness (G, K, J, CTOD, CTOA) testing and standardization, Eng. Fract. Mech. 85 (May 2012) 1–46, https://doi.org/10.1016/j.engfracmech.2012.02.001.
[47] A. Riedl, et al., A novel approach for determining fracture toughness of hard coatings on the micrometer scale, Scripta Mater. 67 (7–8) (Oct. 2012) 708–711, https://doi.org/10.1016/j.scriptamat.2012.06.034.
[48] S. Wurster, C. Motz, R. Pippan, Characterization of the fracture toughness of micro-sized tungsten single crystal notched specimens, Phil. Mag. 92 (14) (May 2012) 1803–1825, https://doi.org/10.1080/14786435.2012.658449.
[49] R. Pan, Y. Chen, H. Lan, S. E, R. Ren, Investigation into the microstructure evolution and damage on rail at curved tracks, Wear 504 (505) (Sep. 2022), 204420, https://doi.org/10.1016/j.wear.2022.204420.
[50] Y. Zhou, J.F. Peng, Z.P. Luo, B.B. Cao, X.S. Jin, M.H. Zhu, Phase and microstructural evolution in white etching layer of a pearlitic steel during rolling–sliding friction, Wear 362 (363) (Sep. 2016) 8–17, https://doi.org/10.1016/j.wear.2016.05.007.
[51] W. Österle, H. Rooch, A. Pyzalla, L. Wang, Investigation of white etching layers on rails by optical microscopy, electron microscopy, X-ray and synchrotron X-ray diffraction, Mater. Sci. Eng., A 303 (1–2) (May 2001) 150–157, https://doi.org/10.1016/S0921-5093(00)01842-6.
[52] W. Lojkowski, M. Djahanbakhsh, G. Bürkle, S. Gierlotka, W. Zielinski, H.-J. Fecht, Nanostructure formation on the surface of railway tracks, Mater. Sci. Eng., A 303 (1–2) (May 2001) 197–208, https://doi.org/10.1016/S0921-5093(00)01947-X.
[53] Robert O. Ritchie, The conflicts between strength and toughness, Nat. Mater. 10 (2011) 817–822.
[54] A. Chabok, E. Van der Aa, J.T.M. De Hosson, Y. Pei, Characterization of Fracture Toughness for Different Zones of Resistance Spot Welded Dual Phase Steel Using Micro-cantilever Testing: International Conference on PROCESSING & MANUFACTURING of ADVANCED MATERIALS, International Conference on PROCESSING & MANUFACTURING OF ADVANCED MATERIALS, Jul. 2018.
[55] B.N. Jaya, Fracture behavior of nanostructured heavily cold drawn pearlitic steel wires before and after annealing, Mater. Sci. 8 (2017).

[56] A. Kumar, et al., In situ study on fracture behaviour of white etching layers formed on rails, Acta Mater. 180 (Nov. 2019) 60–72, https://doi.org/10.1016/j.actamat.2019.08.060.
[57] B. Li, P. Li, R. Zhou, X.-Q. Feng, K. Zhou, Contact mechanics in tribological and contact damage-related problems: a review, Tribol. Int. 171 (Jul. 2022), 107534, https://doi.org/10.1016/j.triboint.2022.107534.
[58] Q. Lian, G. Deng, H. Zhu, H. Li, X. Wang, Z. Liu, Influence of white etching layer on rolling contact behavior at wheel-rail interface, Friction 8 (6) (Dec. 2020) 1178–1196, https://doi.org/10.1007/s40544-020-0388-x.
[59] J. Pan, L. Chen, C. Liu, G. Zhang, R. Ren, Relationship between the microstructural evolution and wear behavior of U71Mn rail steel, J. Mater. Eng. Perform. 30 (2) (Feb. 2021) 1090–1098, https://doi.org/10.1007/s11665-021-05452-6.